Research in Astronomy and Astrophysics, 22:105014 (10pp), 2022 October https://doi.org/10.1088/1674-4527/ac8d7e

Revealing Double White Dwarf Mergers with Multi-messenger Signals

He-Wen Yang[1,2], Pak-Hin Thomas Tam[1,2], and Lili Yang[1,2]
[1] School of Physics and Astronomy, Sun Yat-sen University, Zhuhai 519082, China; tanbxuan@mail.sysu.edu.cn, yanglli5@mail.sysu.edu.cn
[2] CSST Science Center for the Guangdong-Hong Kong-Macau Greater Bay Area, Sun Yat-Sen University, Zhuhai 519082, China
Received 2022 June 26; revised 2022 July 20; accepted 2022 July 26; published 2022 October 4

Abstract

A significant number of double white dwarfs (DWDs) are believed to merge within the Hubble time due to the gravitational wave (GW) emission during their inspiraling phase. The outcome of a DWD system is either a type Ia Supernova as the double-degenerate model, or a massive, long-lasting merger remnant. Expected multi-messenger signals of these events will help us to distinguish detailed merging physical processes. In this work, we aim to provide a generic scenario of DWD merging, investigate the emission of all major messengers, with a focus on GWs and neutrinos. Our goal is to provide some guidance for current and future (collaborative) efforts of multi-messenger observations. Throughout the merging evolution of a DWD system, different messengers (GW, neutrino and electromagnetic wave) will dominate at different times. In this work, we show that DWD merger events located at the distance of 1 kpc can indeed produce detectable signals of GWs and neutrinos. The GW frequency is in 0.3–0.6 Hz band around 10 days before tidal disruption begins. We estimate that in optimistic situations, the neutrino number detected by upcoming detectors such as JUNO and Hyper-Kamiokande can reach O(1) for a DWD merging event at $\sim$1 kpc.

Key words: (stars:) white dwarfs – (stars:) binaries (including multiple): close – neutrinos – gravitational waves

1. Introduction

Many pieces of evidence show that most stars in the Universe are not single isolated stars, but in binary systems (Sana et al. 2012; Duchêne & Kraus 2013; El-Badry et al. 2021). Stellar evolution models suggest that most stars will become white dwarfs (WDs). Therefore, the most common compact object mergers form out of double white dwarf (DWD) binaries.

In the past few years, some studies of DWD mergers show that every close, DWD binary may eventually merge due to energy loss and angular momentum loss through gravitational wave (GW) radiation (Shen 2015). DWD mergers can lead to various kinds of observable astronomical phenomena including some most luminous transient events in the Universe. On one hand, DWDs are treated as one of the progenitors of type Ia Supernovae (SNe Ia) for a long time, known as the double-degenerate (DD) scenario (Yungelson & Kuranov 2016; Livio & Mazzali 2018). Other suggested manifestations of DWD mergers are transient electromagnetic signals such as fast blue optical transients (Lyutikov & Toonen 2019) and less-luminous nova-type explosions (Roy et al. 2022). On the other hand, if the merger core fails to ignite, the merger product is not clear, suggestions include a rapidly rotating WD with a strong magnetic field (Ji et al. 2013; Rueda et al. 2019) which latter collapses to a neutron star (NS) (Ruiter et al. 2019; Liu & Wang 2020), or a heavy, long-lasting WD (Schwab 2021; Wu et al. 2022). Therefore, a full understanding of the outcomes of DWD mergers not only provides us with the merger rates of the most common compact objects in the Universe, it will also help us to understand the origin of a broad range of transient phenomena and the formation of a class of specific WDs and NSs.

DWD systems are important GW sources (Nelemans et al. 2001; Huang et al. 2020). During the inspiral phase, DWD systems are stable, low frequency (1–10 mHz) GW sources, and are expected to be the first detected GW sources for the space-based GW observatories like LISA (Robson et al. 2019), Taiji and TianQin (Gong et al. 2021). In the galaxy, the high number distribution of low-mass (CO-He) DWDs makes them the dominant GW sources at frequency $\geqslant$5 mHz, while massive (CO–CO or ONeMg) DWDs are less numerous, and the former evolve to merge more quickly than the latter after common-envelope phases or stable Roche lobe overflow phase (Yu & Jeffery 2010). However, if they successfully evolve to very close binary (i.e., they tend to merge soon), the GW frequency of the system can reach 0.1 Hz or even 1 Hz (Maselli et al. 2020; Zou et al. 2020).

Neutrinos are believed to be generated from astrophysical sources such as stellar cores, novae, core-collapse supernovae and compact binary mergers at MeV energies or from the cosmic rays accelerators at high and ultra-high energies (Halzen & Hooper 2002; Katz & Spiering 2012; Vitagliano et al. 2020). However, the merging physics of DWDs is still unclear, and few works involving numerical simulations focus on neutrino emission. During the merging stage, the interaction region of DWD can create density and temperature conditions which are high enough

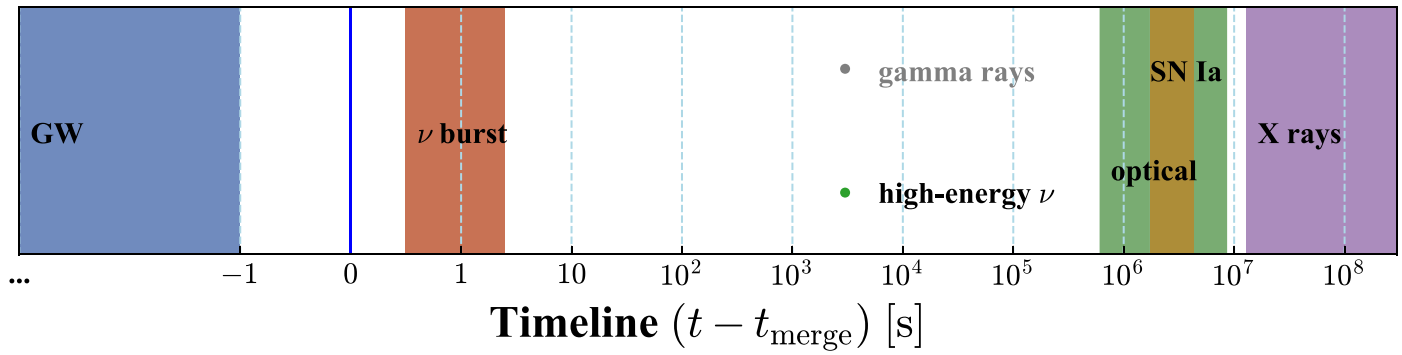

Figure 1. Plausible signals timeline before and after DWD merging in a multi-messenger perspective

for efficient neutrino production such that neutrinos can dominate the carried-away energy (Aznar-Siguán et al. 2014). In recent years, some single-degenerate models indicate that normal SNe Ia bursts can produce significant neutrino flux that is four orders of magnitude smaller than that of core-collapse SNe, regardless of the exact explosion mechanism (Kunugise & Iwamoto 2007; Odrzywolek & Plewa 2011; Seitenzahl et al. 2015; Wright et al. 2017). However, the neutrino flux associated with double-degenerate model has rarely been studied by simulations. It has previously been suggested that neutrino signals could help to distinguish these two progenitor models of SNe Ia (Raj 2020). It is commonly thought that SNe Ia come from the detonation of WD carbon cores when the temperature and density reach the ignition condition. Besides, the neutrino production is efficient when the temperature reaches above 10^9 K, and carbon burning can reach such temperature (Itoh et al. 1996), and in such a case neutrino production will dominate the energy release.

In this work, we investigate the multi-messenger detection prospects of DWDs, focusing on GWs and neutrinos. We mainly focus on the CO DWD systems which are detached binaries. In Section 2, we provide a simple description of DWD merging processes and a schematic overview of possible multi-messenger signals as well as their emission times for a merging event. In Section 3, we assume a toy model for gravitational wave and neutrino production when DWDs merge, introducing some physical quantities to describe the two types of signals. In Section 4, we calculate the amplitude spectral density for the final inspiraling evolution and the neutrino number events from the merging process, and discuss their detectability using current and planned detectors. Finally, we present the discussions and conclusion of our results in Section 5.

2. The Mechanism of Double White Dwarf Mergers

2.1. Physical Processes

In recent years, the merging dynamics of DWDs have been investigated by smoothed particle hydrodynamics (SPH) simulations, which reveal the details of the merging processes (Lorén-Aguilar et al. 2009; Pakmor et al. 2010, 2012; Raskin et al. 2012; Ji et al. 2013; Sato et al. 2015, 2016). In general, it is thought that the less massive WD could be tidally disrupted by the more massive WD that remains. A small amount of mass of the disrupted one, which carries most of the angular momentum, are fast accreted onto the surface of the undisrupted one, forming a thick Keplerian disk.

Depending on the initial masses and mass transfer rate of the DWD, it may result in the immediate ignition of the carbon core of the more massive WD that explodes (a violent merger), or that the product fails to be detonated after they merge. In the latter case, a magnetized corona above the disk and a strongly magnetized bi-conical jets perpendicular to the disk can form because of the development of the magneto-rotational instability within the disk (Ji et al. 2013). A viscous outflow is driven at the interface of the corona and the jet. It is also argued that the merging may go through some viscous processes with a timescale longer than the dynamical timescale, producing SN Ia explosion. Otherwise, if there is no explosion, the merge product is a more massive (ONeMg) WD. Even when the remnant mass exceeds the Chandrasekhar limit, the remnant will undergo a long-term evolution before it finally collapses to form an NS (Schwab 2021).

2.2. Multi-messenger Signals

In Figure 1, we depict anticipated emission signals from DWD merger events. A plausible timeline of the signals associated with various processes is outlined as follows:

1. During the inspiral phase, the emission is dominated by GW. It is believed that GW emission reaches a maximum when tidal disruption occurs and thereafter is largely suppressed.
2. When tidal disruption starts, the dynamical timescale is thought to be ∼1 s as estimated by the freefall motion of the accreting mass across the tidal disruption radius of the secondary.

Table 1
DWD, DNS and DBH Merger Rate in the Local Universe and in the Milky Way

System	$\mathcal{R}$ (Gpc^{-3} yr^{-1})	MW Event Rate ((100 yr)$^{-1}$)	References
DWD	$(0.74-5.94)\times10^{6}$ (2σ)	$0.64-51$	(Maoz & Hallakoun 2017)
DWD	$(5.2\pm1.5)\times10^{5}$ (1σ)	4.5 ± 1.3	
DNS	320^{+490}_{-240}	$2.8^{+4.2}_{-2.1}\times10^{-3}$	(Abbott et al. 2021)
DBH	$23.9^{+14.3}_{-8.6}$	$2.1^{+1.2}_{-0.7}\times10^{-4}$	(Abbott et al. 2021)

3. Subsequently, a neutrino burst with a time duration of $\mathcal{O}$(1 s) follows immediately the dynamical merging process.
4. If SNe Ia explosion occurs, most materials of the DWD is thrown out, giving rise to a supernova light curves that may differ from (and indeed are likely broader than) those in Chandrasekhar-mass explosion models (Fryer et al. 2010; Moll et al. 2014). The luminosity reaches the maximum at ∼30 days after they merge.
5. If there is no explosion, then in the viscous outflow process, cosmic rays are being accelerated via magnetic dissipation in the outflow region, subsequently leading to high-energy neutrino emission $\sim10^{4}$ s after the merge (Xiao et al. 2016). It is also argued that gamma-rays might be produced too, but can hardly be detected because of the surrounding optically thick environment. About ∼7 days, after the merge optical photons are emitted due to the adiabatic cooling of ejecta. In addition, fallback accretion and spindown of the newly-formed central WD will produce X-rays about 150–200 days post-merging (Rueda et al. 2019).

2.3. Merger Rate

The merger rate of DWDs is the highest among all types of merger events in the Universe. In the Milky Way, the merger rate of DWD is expected to be (1–80) $\times$ 10^{-13} yr$^{-1}M_{\odot}^{-1}$ (2σ) or $(7\pm2)\times10^{-13}$ yr$^{-1}M_{\odot}^{-1}$ (1σ) (Maoz & Hallakoun 2017). For comparison, by using the Milky Way stellar mass $6.4\times10^{10}\,M_{\odot}$ and the extrapolating factor of Milky Way-type galaxies 1.16×10^{-2} Mpc^{-3} (Kalogera et al. 2001) for DWDs, the merger rates of double neutron stars (DNSs) and double black holes (DBHs) are shown in Table 1, which are smaller than DWDs by 2–4 orders of magnitude. Additionally, previous studies also show that DWD merger rates are consistent and on the same order of SNe Ia rates deduced from observations (Toonen et al. 2012; Maoz et al. 2014, 2018).

3. A Multi-messenger Perspective of Double White Dwarf Mergers

In this section, we focus on the anticipated GW and neutrino emission from a DWD merging event.

3.1. Gravitational Waves

In this work, we assume that there is neither mass-transfer nor interaction between the two WDs until tidal disruption happens, because we assume that both components of the binary are of the type CO-WD or even more massive (ONeMg) WD. It is therefore reasonable to assume a two point-mass approximation during the inspiral phase.

Considering a DWD system with component masses m_1 and m_2 and an orbital separation of a, the orbital frequency is derived from its Keplerian motion as:

$$f_{\rm orb}=\sqrt{\frac{G(m_1+m_2)}{2\pi^2a^3}}, \tag{1}$$

where G is the gravitational constant. In the case of a circular orbit, the GW is radiated only in the second harmonics, and hence the GW frequency f is twice that of the orbital frequency $f=2f_{\rm orb}$. During the inspiraling phase, the two independent polarization states (or waveforms) $+$ and $\times$ of GW radiation from DWD in the quadrupole approximation (Landau & Lifshitz 1962) is

$$h_{+}=\frac{(G\mathcal{M}_c)^{5/3}}{c^4d}(\pi f)^{2/3}2(1+\cos^2 i)\cos(2\pi ft), \tag{2}$$

$$h_{\times}=\frac{(G\mathcal{M}_c)^{5/3}}{c^4d}(\pi f)^{2/3}4\cos i\sin(2\pi ft). \tag{3}$$

where c is the speed of light, $\mathcal{M}_c=(m_1m_2)^{3/5}/(m_1+m_2)^{1/5}$ is the chirp mass and d is the distance to the source. The GW emission luminosity is:

$$L_{\rm GW}=\dot{E}=\frac{32}{5}\frac{G^4}{c^5}\frac{m_1^2m_2^2(m_1+m_2)}{a^5}. \tag{4}$$

Alternatively, it can be expressed as a function of chirp mass and GW frequency

$$L_{\rm GW}=\frac{32}{5}\frac{G^{7/3}}{c^5}(\pi f\mathcal{M}_c)^{10/3}. \tag{5}$$

Due to GW emission loss, the GW frequency evolves as:

$$\dot{f}=\frac{96}{5\pi}\frac{(G\mathcal{M}_c)^{5/3}}{c^5}(\pi f)^{11/3}. \tag{6}$$

Introducing the strain amplitude h_0 (or the instantaneous root-mean-square amplitude),

$$h_0 = \sqrt{\langle h_+^2 \rangle + \langle h_\times^2 \rangle} = \sqrt{\frac{32}{5}} \frac{(G\mathcal{M}_c)^{5/3}}{c^4 d} (\pi f)^{2/3}. \quad (7)$$

Averaging over a full orbital period and all inclination angle, it is related to the GW luminosity by (Postnov & Yungelson 2014)

$$h_0^2 = \frac{1}{(\pi d)^2} \frac{G}{c^3} \frac{L_{\rm GW}}{f^2}. \quad (8)$$

The characteristic strain amplitude h_c for inspiraling binaries is given by (Finn & Thorne 2000; Moore et al. 2014)

$$h_c^2 = \left(\frac{2f^2}{\dot{f}} \right) h_0^2 = \frac{2}{3} \frac{(G\mathcal{M}_c)^{5/3}}{c^3 d^2} f (\pi f)^{-4/3}. \quad (9)$$

The amplitude spectral density (ASD) is defined as $\sqrt{S_h} = h_c f^{-1/2}$, where S_h is the power spectral density of sources (Moore et al. 2014). Similarly, for GW detectors, $\sqrt{S_N(f)}$ is the effective strain spectral density of the detector noise used in sensitivity curves (Robson et al. 2019; Huang et al. 2020).

Inspiraling of compact binaries can be well-modeled in theoretical analysis while the merging of binaries (especially those bursting sources) is poorly modeled (Moore et al. 2014). As mentioned above, we consider the binary evolution during the inspiral phase, during which GW frequency is slowly changing $\Delta f = \dot{f}\,\Delta t$, and the GW signal is weak and remains almost unchanged for many years, then the corresponding signal is accumulated at detectors over a long time Δt, increasing the signal-to-noise ratio (SNR). The ASD can be described as $\sqrt{S_h} = \sqrt{2}\, h_0 \sqrt{\Delta t}$. However, for latter phases of DWD evolution (i.e., right before the tidal disruption), the frequency and strain is enhanced within a very short time (e.g., several orbital periods), they can be treated as burst sources. These systems produce large amplitude signals that could be much higher than the detector noise and specific waveform models are not necessary in signal detection. In practice, the signal amplitude described for burst sources is the root-sum-square amplitude

$$h_{\rm rss}^2 = \int {\rm d}t\, (|h_+(t)|^2 + |h_\times(t)|^2). \quad (10)$$

It can be approximated to $h_{\rm rss} \simeq |\tilde{h}(f)| \sqrt{\Delta f}$ by assuming that the GW mode is linearly polarized and $|\tilde{h}(f)|$ is almost constant within a frequency band Δf, where $\tilde{h}(f)$ is the Fourier transform of $h(t)$. However, the quantity $h_{\rm rss}$ is on the same order as the characteristic strain h_c as defined before (Moore et al. 2014). In this work, the main phase that we focused on is the last stages of inspiraling before tidal disruption, and we therefore use h_c to represent GW emission.

3.2. Neutrinos

3.2.1. Neutrino Production

We now consider neutrino emission from the merger event. When the density and temperature are high enough, thermal neutrino processes begin and produce $\mathcal{O}(1)$ MeV neutrinos, at the same time neutrino cooling becomes efficient. In general, five thermal neutrino processes are taken into account: electronpositron annihilation, plasmon decay, photoemission, neutrino Bremsstrahlung and recombination, which produce neutrinos with all kinds of flavors (Itoh et al. 1996). Once the temperature exceeds 10^9 K, electronpositron annihilation

$$e^+ + e^- \rightarrow \nu + \bar{\nu}, \quad (11)$$

starts to dominate the thermal neutrino production (Itoh et al. 1996).

When the merging process is violent, the temperature can easily reach $\geqslant 5 \times 10^9$ K such that weak processes including electron and positron capture become more efficient than thermal neutrino production channels. These weak processes mainly produce electron neutrinos and anti-electron neutrinos via,

$$p + e^- \rightarrow n + \nu_e, \quad (12)$$

$$n + e^+ \rightarrow p + \bar{\nu}_e, \quad (13)$$

$$(Z, A) + e^- \rightarrow (Z - 1, A) + \nu_e, \quad (14)$$

$$(Z - 1, A) + e^+ \rightarrow (Z, A) + \bar{\nu}_e. \quad (15)$$

During the DWDs merging process, the material is proton-rich so that the electron capture happens mainly between free protons/nuclei and electrons, resulting in a dominant ν_e emission.

We assume that neutrinos follow the Fermi–Dirac distribution with zero chemical potential, and the neutrino number emitted per energy per time per area could be written as

$$\Phi_\nu(E) = \frac{L_\nu}{4\pi d^2} \frac{120}{7\pi^2} \frac{E^2}{T^4} \frac{1}{1 + e^{E/k_B T}}, \quad (16)$$

where L_ν is the neutrino luminosity, T the neutrino temperature, E the neutrino energy and d the distance to the Earth. Here we take the average neutrino energy to be $\langle E \rangle \sim 3.15 k_B T$, a result from the Fermi–Dirac distribution.

Neutrino luminosity and average energy strongly depend on the merging processes. Dynamical interactions of DWD failing to ignite can result in optimistic values of neutrino luminosity with the total energy $\sim 10^{48}$ erg (Aznar-Siguán et al. 2014). As mentioned before, SNe Ia can produce a large amount of neutrinos (Kalogera et al. 2001; Wright et al. 2017), so it should be reasonable to assume that SNe Ia from the double-degenerate channel can also generate a neutrino burst with the luminosity $\sim 10^{49}$ erg s^{-1} or even $\sim 10^{50}$ erg s^{-1}. Here we adopt three characteristic temperature values in our study:

Table 2
The Neutrino Luminosity, Duration time and Temperature we Adopt in this Work

Cases	L_{ν_e} (erg s^{-1})	Δt (s])	T (K)	Reference
Case 1	10^{50}	1	$\langle E\rangle = 3$ MeV	(Kunugise & Iwamoto 2007)
Case 2	10^{49}	2	4×10^{9}	(Wright et al. 2017)
Case 3(a)	10^{48}	1	10^{10}	
Case 3(b)	10^{48}	1	4×10^{9}	(Aznar-Siguán et al. 2014)
Case 3(c)	10^{48}	1	10^{9}	

1. $\geqslant 10^9$ K: this is above the carbon burning temperature, electron-positron pair annihilation starts to dominate the thermal production process;
2. around 4×10^9 K: nuclear statistical equilibrium (NSE) starts, and the electron capture process becomes efficient;
3. around 10^{10} K: it is the typical core neutrino temperature in an SN Ia explosion, resulting in the neutrino average energy $\langle E\rangle \sim 3$ MeV.

During the neutrino burst, the weak or thermal production processes happen. For weak processes, the timescale of NSE can be approximated as $\tau_{\rm NSE}\sim 1$ s for SNe Ia explosion (Kunugise & Iwamoto 2007), which is the same order as the explosion timescale. Assuming that DWDs merging could also reach the NSE condition (i.e., Cases 1, 2, 3(a), and 3(b)), it would be reasonable to assume that it also lasts for about 1 second. While in the thermal production, which is related to density and temperature during the merge processes, we assume that it lasts $\sim$1 s, to be consistent with the case of explosion. The neutrino luminosity L_ν, emission duration Δt and temperature T are assumed in this work as shown in Table 2. In Table 2, we argue that Cases 1 and 2 likely represent situations which will lead to SNe Ia, and neutrinos carry away $\sim$(1–10)% of the total released energy of 10^{51} erg. For Cases 3(a), 3(b) and 3(c), the luminosity is lower compared with the SNe Ia case, and we consider cases with temperature values (i.e., 4×10^9 K or even 10^{10} K) which are somewhat optimistic.

Based on the assumed parameter values as in Table 2, the respective neutrino flux values are calculated with Equation (16). From Figure 2, for higher temperature (averaged energy), the distribution of neutrino (flux) has broader energy range.

Here, the material is proton-rich (electron fraction $Y_e > 0.5$) during DWD merge, it implies that electron capture dominates neutrino production process, and ν_e will be dominant during the emission.[3] Nevertheless, it is a neutronization process which losses lepton number by neutrino release (nucleosynthesis that produce heavier elements also occurs). On the other hand, if the thermal burning process dominates, neutrinos of all flavors will be produced with similar proportions. However, if weak processes become significant, then the production rates of thermal processes become sub-dominant at the same physical conditions, thus the thermal contribution to the neutrino flux can be safely ignored. We note also that no neutrino trapping is expected to occur in core-collapse supernovae, because the matter density of DWD merger is not high enough.[4]

3.2.2. Neutrino Oscillation Effects

From the production region to surface, neutrino flavors will be regulated by the Mikheyev–Smirnov–Wolfenstein (MSW) effect (Wolfenstein 1978; Mikheyev & Smirnov 1985; Blennow & Smirnov 2013). These regulations are different depending on the mass order hierarchy: the normal mass hierarchy (NH) or the inverted mass hierarchy (IH) (Dighe & Smirnov 2000; Fogli et al. 2005). If we denote the initial flux as $\Phi^0_{\nu_\alpha}$ ($\Phi^0_{\bar\nu_\alpha}$) where $\alpha = e,\ \mu,\ \tau$, then with the MSW resonance effect, the flux at the surface is Φ_{ν_α} ($\Phi_{\bar\nu_\alpha}$). When neutrinos propagate from the source surface to the Earth, neutrino oscillation in vacuum has to be taken into account. The neutrino fluxes observed ϕ_{ν_α} ($\phi_{\bar\nu_\alpha}$) are different from Φ_{ν_α} ($\Phi_{\bar\nu_\alpha}$). In general, the transition probabilities between ϕ_{ν_α} ($\phi_{\bar\nu_\alpha}$)and Φ_{ν_α} ($\Phi_{\bar\nu_\alpha}$) is:

$$\phi_{\nu_\beta}(E) = \sum_\alpha \Phi_{\nu_\alpha}(E) P_{\nu_\alpha\to\nu_\beta}(L/E), \tag{17}$$

$$\phi_{\bar\nu_\beta}(E) = \sum_\alpha \Phi_{\bar\nu_\alpha}(E) P_{\bar\nu_\alpha\to\bar\nu_\beta}(L/E), \tag{18}$$

i.e., it depends on the energy of the neutrinos and their travel distance (evolution time). However, the astrophysical sources are so far way from the Earth, so the probabilities should be averaged along the way and can be described as

$$P_{\alpha\beta} = \langle P_{\nu_\alpha\to\nu_\beta}\rangle = \sum_i^3 |U_{\alpha i}|^2 |U_{\beta i}|^2, \tag{19}$$

$$\bar P_{\alpha\beta} = \langle P_{\bar\nu_\alpha\to\bar\nu_\beta}\rangle = P_{\alpha\beta}, \tag{20}$$

where $U_{\alpha i}$ is the element of Pontecorvo-Maki-Nakagawa-Sakata (PMNS) mixing matrix (Pontecorvo 1957; Maki et al. 1962)

$$U = \begin{pmatrix} c_{12}c_{13} & s_{12}c_{13} & s_{13}e^{-i\delta} \\ -s_{12}c_{23} - c_{12}s_{23}s_{13}e^{i\delta} & c_{12}c_{23} - s_{12}s_{23}s_{13}e^{i\delta} & s_{23}c_{13} \\ s_{12}s_{23} - c_{12}c_{23}s_{13}e^{i\delta} & -c_{12}s_{23} - s_{12}c_{23}s_{13}e^{i\delta} & c_{23}c_{13} \end{pmatrix}, \tag{21}$$

where $s_{ij} = \sin\theta_{ij}$, $c_{ij} = \cos\theta_{ij}$, in which θ_{ij} is the lepton flavor mixing angle and δ is the CP violation phase. The above parameters are taken from Zyla et al. (2020).

[3] Meanwhile in DNS merge $\bar\nu_e$ dominates due to positron capture in neutron-rich matters.

[4] Core-collapse supernovae are triggered by massive star collapse. Before the explosion, the center core of star is so dense ($\geqslant 10^{11}$ g cm^{-3}) that neutrinos cannot escape and are trapped in the inner regions for some time. Only after the explosion starts, the core density decreases and the trapping conditions do not exist any more, leading to a neutrino burst.

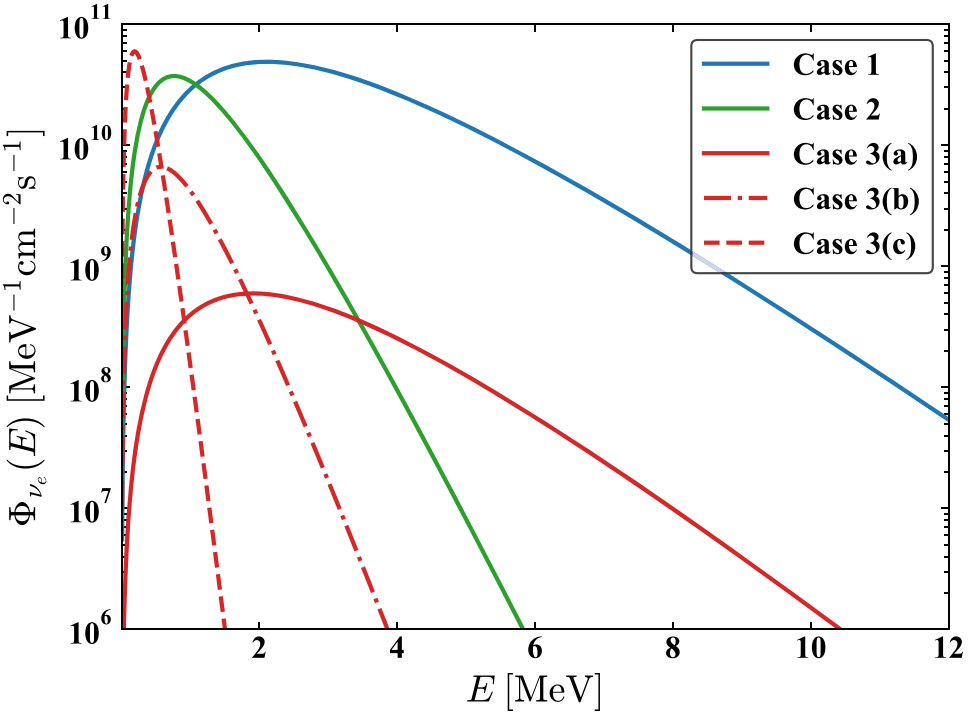

Figure 2. Neutrino fluxes of five cases presented in Table 2, and the distance from the source is $d = 1$ kpc.

For the situation of electron neutrino dominant, $\Phi^0_{\nu_e}: \Phi^0_{\nu_x}: \Phi^0_{\bar{\nu}_e}: \Phi^0_{\bar{\nu}_x} = 1: 0: 0: 0$, it leads to $\phi_{\nu_e}: \phi_{\nu_x}: \phi_{\bar{\nu}_e}: \phi_{\bar{\nu}_x} = 0.23: 0.77: 0: 0$ for NH case and $0.32: 0.68: 0: 0$ for IH case. Here, the subscript e and x denote the electron flavor and other (μ and τ) flavors, and the bar denote the antineutrinos with different types. If three flavors of neutrinos are equally emitted, i.e., $\Phi^0_{\nu_e}: \Phi^0_{\nu_x}: \Phi^0_{\bar{\nu}_e}: \Phi^0_{\bar{\nu}_x} = 1/6: 1/3: 1/6: 1/3$, it has a trivial effect $\phi_{\nu_e}: \phi_{\nu_x}: \phi_{\bar{\nu}_e}: \phi_{\bar{\nu}_x} = 1/6: 1/3: 1/6: 1/3$. In this case, the neutrino mass order hierarchy cannot be distinguished.

4. Detectability

4.1. Gravitational Waves

The power of GW emission reaches the maximum when tidal disruption occurs and is largely suppressed when the secondary mass starts to be disrupted. We assume that the merging process occurs when the orbital separation a_m is equal to the tidal disruption radius:

$$a_m = R_{\rm td} = qR_2 \tag{22}$$

where q, R_2 is the mass-ratio (m_2/m_1) and the radius of the secondary WD, respectively. We assume the WD radius to be:

$$R \approx \sqrt[3]{\frac{3m}{4\pi\rho}}, \tag{23}$$

where ρ is the mean density of WD. The final cut-off GW frequency is then determined by Equation (1).

In this work, we consider four hypothetical DWD systems: $(1.0+0.8)M_\odot$, $(1.0+1.0)M_\odot$, $(1.1+0.9)M_\odot$ and $(1.2+1.0)M_\odot$ which are usually assumed in simulations and might mostly lead to SNe Ia, which also have a high probability to produce neutrinos with significant luminosity. For various masses, the mean densities are taken to be $10^6\,{\rm g\,cm^{-3}}$ (for $0.8\,M_\odot$), $2\times10^6\,{\rm g\,cm^{-3}}$ (for $0.9\,M_\odot$) and $3\times10^6\,{\rm g\,cm^{-3}}$ (for $1.0\,M_\odot$), which we refer to Figure 1 of Zou et al. (2020).

Here, we use the Python package LEGWORK[5] (Wagg et al. 2021) to calculate the strain amplitude h_0 and characteristic strain amplitude h_c of binaries systems and the evolution of their orbital frequency $f_{\rm orb}$. LEGWORK is also used to calculate SNRs of GW emitted from inspiraling binary systems as detected by certain GW detectors. However, in this work, we mainly focus on the latter stage of DWD merging process. We also take the initial GW frequency to be 5 mHz for four systems, and follow the evolution of GW frequency based on the two-point approximation as described in Section 3.1.

Figure 3 shows the luminosities of GW emission $L_{\rm GW}$ for these systems from 10 days before tidal disruption, $t_{\rm td}$, to the time of disruption. It can be seen that for more massive systems, the luminosities are higher as expected. With the same total mass, the equal mass-ratio (e.g., $(1.0+1.0)M_\odot$) system has a smaller luminosity than the unequal mass-ratio (e.g., $(1.1+0.9)M_\odot$) one. Integrating luminosities from $t_{\rm td}-10$ day

[5] https://legwork.readthedocs.io/en/latest/

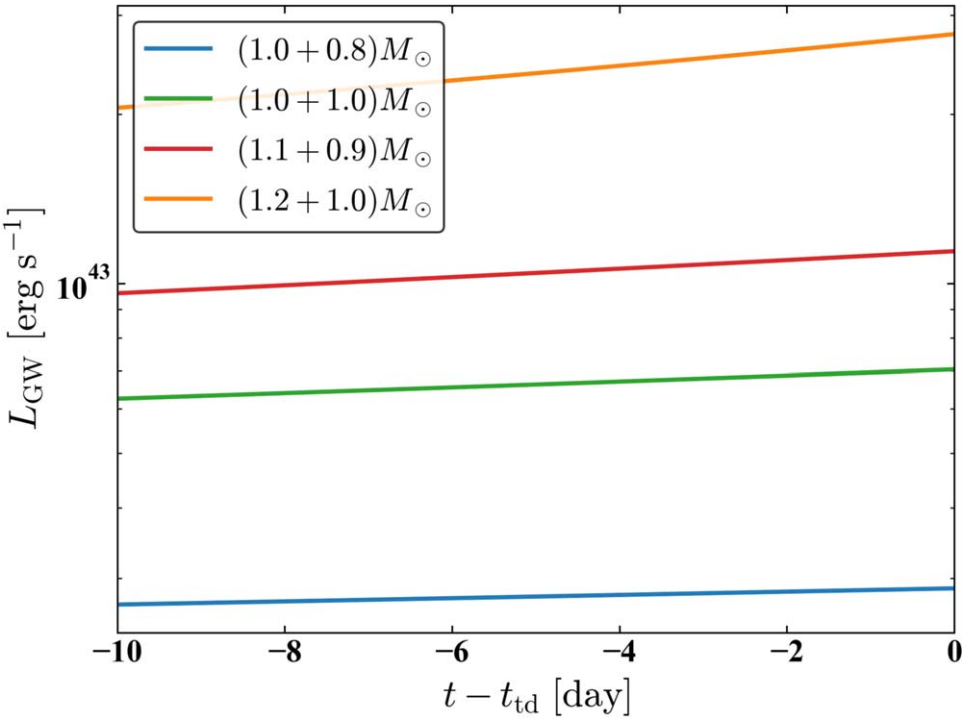

Figure 3. The GW luminosity in final evolution phase (i.e., beginning 10 days before the tidal disruption). The line colors denote systems with different component masses: $(1.0 + 0.8)M_\odot$, $(1.0 + 1.0)M_\odot$, $(1.1 + 0.9)M_\odot$ and $(1.2 + 1.0)M_\odot$.

to $t_{\rm td}$, it follows that the energy release by GW emission is on the order of 10^{48}–10^{49} erg.

We assume the distance from source to the Earth to be 1 kpc, and calculate h_0 and h_c which could represent the instantaneous moment and *accumulated* strength of GW emission. We show the evolution of h_0 and GW frequency of these systems since 10 days before tidal disruption in Figure 4. It can be seen that h_0 and GW frequency are not evolving with the same rate of change, i.e., the latter is changing more rapidly. It implies that the strain amplitude varies across the frequency band in the final stage of merging. Besides, the h_0 and f of DWDs are *slightly* increasing whereas in the cases of DNSs and DBHs they change suddenly. This contrast can be understood because the components of binaries are more compact and have smaller radii in the latter cases. Thus, the cut-off frequencies and the evolution rates of the late stage are larger. On the other hand, the merge of DWD seems gentle comparing with DNSs and DBHs. Nevertheless, the GW signals will be detected by planned space-based interferometers assuming a distance of 1 kpc.

Concerning the detectability of the GW signal, it is a common practise to compare the ASD $\sqrt{S_h}$ with the sensitivity curves of detectors where S_h represents the energy density. Because we are only concerned about the final stage of inspiraling, we can safely ignore the galactic confusion noise which is related to detector's observing time. From Figure 5, if the sources is at the distance of 1 kpc, it is clear that the four systems we assume have a significant signal strength that is easily detected by LISA (Robson et al. 2019) and TianQin (Huang et al. 2020) in 0.3–0.6 Hz frequency band within final 10 days before tidal disruption. We do not calculate the related SNRs because they are so large and the noise is unimportant due to the short time duration in our consideration.

4.2. Neutrinos

Neutrinos from DWD merger events are in the MeV energy scale and are observable via inverse beta decay (IBD) and electron-neutrino elastic scattering (ES) channels. The IBD channel is typically used to detect $\bar{\nu}_e$, while the ES channel is used to detect ν_e and other types of neutrinos. The threshold energy of the IBD channel is ∼1.8 MeV, while that of the ES channel heavily depends on the material used in the detectors. For water Cherenkov detectors such as Super-Kamiokande (Super-K) (Abe et al. 2016) and Hyper-Kamiokande (Hyper-K) (Abe et al. 2018), the threshold energy of recoil electrons is ∼0.77 MeV, corresponding to a minimum neutrino energy of ∼0.97 MeV. The fiducial volume of the inner detector of Super-K and Hyper-K is 22.5 kt and 220 kt, respectively. The corresponding target particle number is $N_{\rm tar} \approx (M_{\rm tar}/m_p) \times (2/18) = 6.7 \times 10^{30}(M_{\rm tar}/1\,{\rm kt})$, where $M_{\rm tar}$ is the effective mass of water and m_p is the proton mass. Therefore, the target

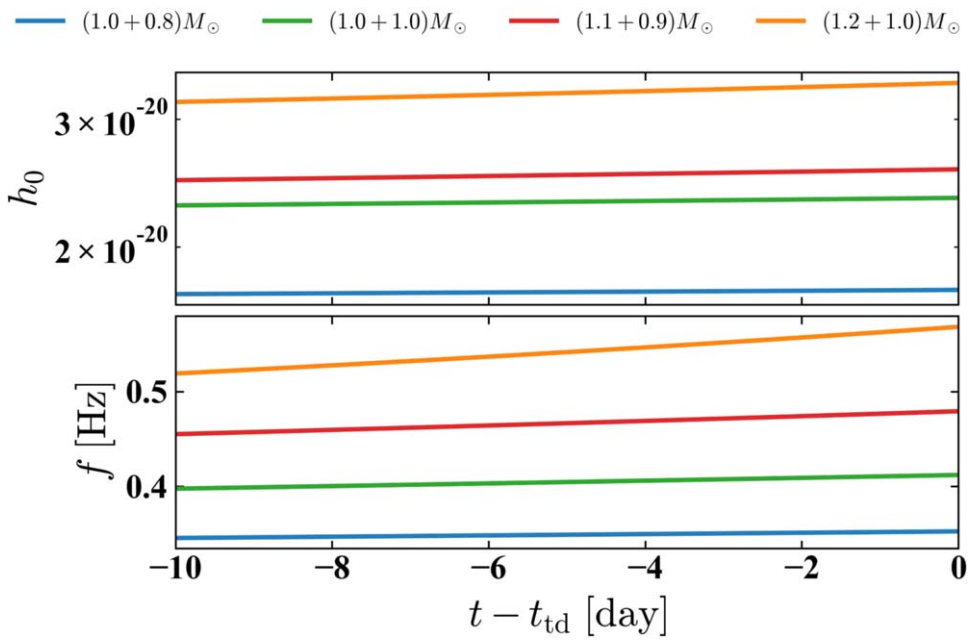

Figure 4. The final evolution of strain amplitude h_0 and GW frequency f beginning 10 days before the tidal disruption. The line colors represent the same systems as in Figure 3.

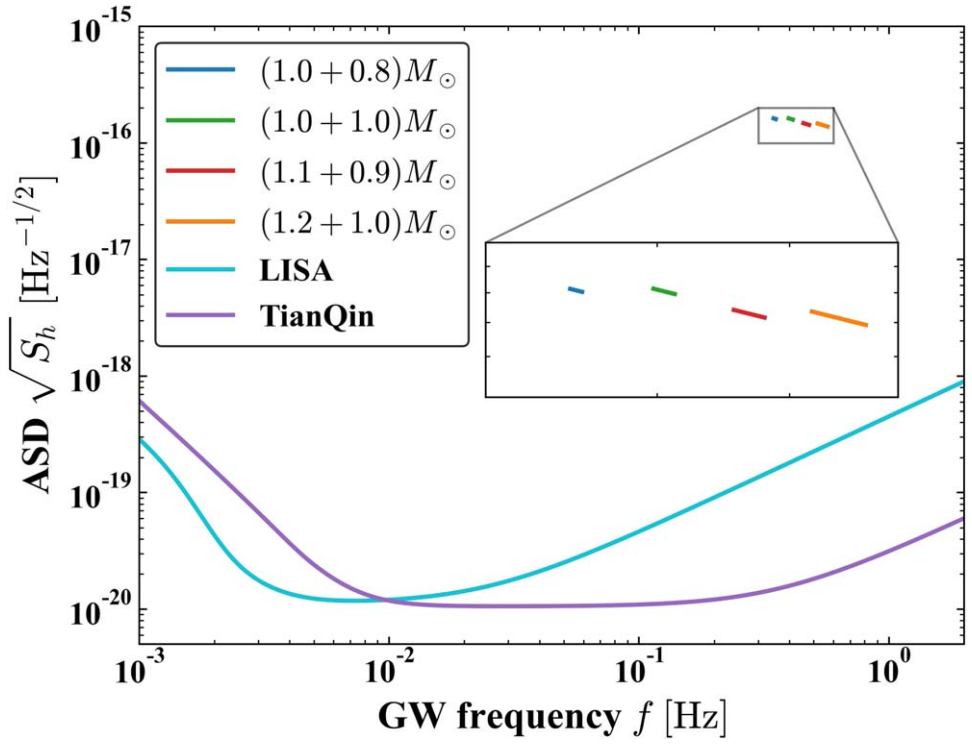

Figure 5. The GW amplitude spectral density (ASD) of the four systems as presented in Figure 3. The sensitivity curves of LISA and TianQin are also shown in this figure. The GW frequency in these cases is in 0.3–0.6 Hz band which can be well detected by space-based GW detectors. Here we assume that the source is 1 kpc away from the Earth.

Table 3
The Electron Neutrino ν_e (other Neutrino ν_x) Events Number Calculated in Detectors Sensitive to $\mathcal{O}$(1 MeV)

Detector	hierarchy	Case 1	Case 2	Case 3(a)	Case 3(b)	Case 3(c)
JUNO	NH	1.2E-00	2.0E-01	1.2E-02	9.8E-03	1.6E-03
		(7.2E-01)	(1.3E-01)	(7.2E-03)	(6.7E-03)	(1.2E-03)
	IH	1.6E-00	2.7E-01	1.6E-02	1.4E-02	2.2E-03
		(6.4E-01)	(1.2E-01)	(6.4E-03)	(6.0E-03)	(1.1E-03)
Super-K	NH	1.4E-01	1.8E-02	1.3E-03	8.9E-04	5.0E-06
		(8.4E-02)	(1.2E-02)	(8.3E-04)	(6.0E-04)	(3.5E-06)
	IH	1.9E-01	2.5E-02	1.9E-03	1.2E-03	7.0E-06
		(7.4E-02)	(1.1E-02)	(7.3E-04)	(5.3E-04)	(3.1E-06)
Hyper-K	NH	1.3E-00	1.7E-01	1.3E-02	8.7E-03	4.9E-05
		(8.2E-01)	(1.2E-01)	(8.1E-03)	(5.8E-03)	(3.4E-05)
	IH	1.8E-00	2.4E-01	1.8E-02	1.2E-02	6.8E-05
		(7.2E-01)	(1.0E-01)	(7.2E-03)	(5.1E-03)	(3.0E-05)

Note. NH and IH denotes the normal and inverted mass order hierarchy for neutrino respectively. In this table, the values are presented in scientific notation and values in bracket are for ν_x.

electron numbers of Super-K and Hyper-K are, respectively, 1.51×10^{32} and 1.47×10^{33}. For JUNO—a liquid organic scintillation, the target number is 1.29×10^{33} (An et al. 2016) with a rather low detection energy threshold of 0.2 MeV (Fang et al. 2020) that corresponds to the neutrino threshold energy of 0.35 MeV. The cross-section of IBD and ES interaction channels are taken from the code package provided by Kate et al. (2017), and the formulae of IBD and ES are taken from Strumia & Vissani (2003); Marciano & Parsa (2003). In this work, ν_e dominates the emission, so we mainly focus on the ES channel.

The neutrino event number can be calculated with

$$N_\nu = N_{\rm tar}\Delta t \int_{E_{\rm th}}^{E_{\rm max}} \phi(E)\sigma(E)\eta(E){\rm d}E, \quad (24)$$

where $N_{\rm tar}$ is the target particle number of protons, Δt denotes the event duration (observed time window), $\sigma(E)$ is the interaction-channel cross section, $\phi(E)$ is neutrino fluxes at earth, $\eta(E)$ is the efficiency of neutrino detector and is usually taken as $\eta \simeq 0.9$.

We could calculate the neutrino numbers and show them in Table 3. From Table 3, one can see that in the most optimistic situation (Case 1), the neutrino number N_{ν_e} (N_{ν_x}) can reach about 2 (at the order of $\mathcal{O}(1)$). N_ν is different between NH and IH, i.e., the ratio of NH and IH ($N_{\rm NH}/N_{\rm IH}$) is 0.72 for ν_e and 1.13 for ν_x. The neutrino event number of Case 3(c) is very small because the average energy of this case are around the threshold of water Cherenkov detectors. It is clear that the higher temperature of neutrinos, the more events we observe in detectors. Furthermore, if the evolution of luminosity is specified, one could expect that the event numbers evolve with time, which reflects the physics of merge processes, particularly the explosion mechanism if it leads to an SN Ia. However, these processes and mechanisms are still poorly studied, and we simply take the average of luminosity with $\Delta t \sim 1$ s time window. Nevertheless, it means that the neutrino production processes are important ingredients in understanding the merging physics.

5. Discussion and Conclusions

In this work, we show that DWD merger events are able to produce detectable GW and neutrino signals if they are located at distance 1 kpc. From GW point of view, the GW frequency DWD systems are within 0.3–0.6 Hz band in 10 days before the tidal disruption in the four example DWD systems that we have studied. Unlike DNSs and DBHs, which are the main potential sources of ground-based GW detectors such as the Advanced LIGO and Virgo, DWD systems are more easily to be detected by space-based GW detectors such as LISA and TianQin at the last stage of inspiraling. Besides, the evolution of strains and GW frequency are moderate while for DNSs and DBHs they are more dramatic. This can be understood since WD are not so dense and the GW signals reach the maximum at tidal disruption radius and thereafter the two bodies merge. The amplitude spectral density of these systems are large comparing to the sensitive curves of LISA and TianQin for the final short time interval, implying that DWDs merging could be well detected by space-based GW detectors.

From neutrino point of view, given that the average energy from these events is $\mathcal{O}(1)$ MeV, the upper limit of neutrino event numbers is on the order of $\mathcal{O}(1)$ for current and upcoming detectors such as Super-K, Hyper-K and JUNO. We found that the merger remnant cases (i.e., Cases 3(a), (b) and (c)) are harder to detect because of the lower neutrino luminosity. In $\mathcal{O}(1)$ MeV energy, the background mainly comes from solar neutrinos but it can be easily removed given the short duration

time. We also show that the detected neutrino flux could help to distinguish the neutrino mass order hierarchy when taking the neutrino oscillation into account. Therefore, we need detectors with larger volume (i.e., more target number) and lower energy threshold, which will also extend the detection horizon distance. More theoretical studies about merging physics and explosion mechanisms of DWDs are also necessary to provide the neutrino luminosity, spectra and oscillation mode.

In the era of multi-messenger astronomy, the DWD merging events are important sources and can be studied using various multi-messenger emissions. Apart from GW and neutrino signals, the subsequent electromagnetic signals such as optical-infrared, X-rays and bolometric light curves are also interesting and important observable signatures (Aznar-Siguán et al. 2014; Moll et al. 2014; Rueda et al. 2019). Even if the electromagnetic signal could be similar between different explosion mechanisms (e.g., DD and SD SNe Ia) and/or merging processes, the neutrino detection can help to distinguish theoretical scenarios once the neutrino production models of DWDs merging are specified. The detection of these sources can join the next-generation supernova early warning system (SNEWS 2.0) (Al Kharusi et al. 2021), and will guide the observation of DWD merging events in the future.

Acknowledgments

This work is supported by the National Natural Science Foundation of China (NSFC, Grant Nos. 11633007, 12005313 and U1731136), Guangdong Major Project of Basic and Applied Basic Research (Grant No. 2019B030302001), Key Laboratory of TianQin Project (Sun Yat-sen University) of the Ministry of Education, and the China Manned Space Project (No. CMS-CSST-2021-B09).

References

Abbott, R., Abbott, T. D., Abraham, S., et al. 2021, ApJL, 913, L7
Abe, K., Abe, K., Aihara, H., et al. 2018, arXiv:1805.04163
Abe, K., Haga, Y., Hayato, Y., et al. 2016, APh, 81, 39
Al Kharusi, S., BenZvi, S. Y., Bobowski, J. S., et al. 2021, NJPh, 23, 031201
An, F., An, G., An, Q., et al. 2016, JPhG, 43, 030401
Aznar-Siguán, G., García-Berro, E., Magnien, M., & Lorén-Aguilar, P. 2014, MNRAS, 443, 2372
Blennow, M., & Smirnov, A. Y. 2013, AdHEP, 2013, 972485
Dighe, A. S., & Smirnov, A. Y. 2000, PhRvD, 62, 033007
Duchêne, G., & Kraus, A. 2013, ARA&A, 51, 269
El-Badry, K., Rix, H.-W., & Heintz, T. M. 2021, MNRAS, 506, 2269
Fang, X., Zhang, Y., Gong, G., et al. 2020, JInst, 15, P03020
Finn, L. S., & Thorne, K. S. 2000, PhRvD, 62, 124021
Fogli, G. L., Lisi, E., Mirizzi, A., & Montanino, D. 2005, JCAP, 2005, 002
Fryer, C. L., Ruiter, A. J., Belczynski, K., et al. 2010, ApJ, 725, 296
Gong, Y., Luo, J., & Wang, B. 2021, NatAs, 5, 881
Halzen, F., & Hooper, D. 2002, RPPh, 65, 1025
Huang, S.-J., Hu, Y.-M., Korol, V., et al. 2020, PhRvD, 102, 063021
Itoh, N., Hayashi, H., Nishikawa, A., & Kohyama, Y. 1996, ApJS, 102, 411
Ji, S., Fisher, R. T., García-Berro, E., et al. 2013, ApJ, 773, 136
Kalogera, V., Narayan, R., Spergel, D. N., & Taylor, J. H. 2001, ApJ, 556, 340
Kate, S., Joshua, B., Justin, V., Felix, M., & Erin, C. 2017, SuperNova Observatories with GLoBES (accessed April 26, 2022), https://github.com/SNOwGLoBES/snowglobes
Katz, U. F., & Spiering, C. 2012, PrPNP, 67, 651
Kunugise, T., & Iwamoto, K. 2007, PASJ, 59, L57
Landau, L. D., & Lifshitz, E. M. 1962, The Classical Theory of Fields, Course of Theoretical Physics (2nd edn.; London: Pergamon) trans. from the Russian
Liu, D., & Wang, B. 2020, MNRAS, 494, 3422
Livio, M., & Mazzali, P. 2018, PhR, 736, 1
Lorén-Aguilar, P., Isern, J., & García-Berro, E. 2009, A&A, 500, 1193
Lyutikov, M., & Toonen, S. 2019, MNRAS, 487, 5618
Maki, Z., Nakagawa, M., & Sakata, S. 1962, PTEP, 28, 870
Maoz, D., & Hallakoun, N. 2017, MNRAS, 467, 1414
Maoz, D., Hallakoun, N., & Badenes, C. 2018, MNRAS, 476, 2584
Maoz, D., Mannucci, F., & Nelemans, G. 2014, ARA&A, 52, 107
Marciano, W. J., & Parsa, Z. 2003, JPhG, 29, 2629
Maselli, A., Marassi, S., & Branchesi, M. 2020, A&A, 635, A120
Mikheyev, S. P., & Smirnov, A. Y. 1985, YaFiz, 42, 1441
Moll, R., Raskin, C., Kasen, D., & Woosley, S. E. 2014, ApJ, 785, 105
Moore, C. J., Cole, R. H., & Berry, C. P. L. 2014, CQGra, 32, 015014
Nelemans, G., Yungelson, L. R., & Portegies Zwart, S. F. 2001, A&A, 375, 890
Odrzywolek, A., & Plewa, T. 2011, A&A, 529, A156
Pakmor, R., Kromer, M., Röpke, F. K., et al. 2010, Natur, 463, 61
Pakmor, R., Kromer, M., Taubenberger, S., et al. 2012, ApJL, 747, L10
Pontecorvo, B. 1957, Zh. Eksp. Teor. Fiz, 34, 247
Postnov, K. A., & Yungelson, L. R. 2014, LRR, 17, 3
Raj, N. 2020, PhRvL, 124, 141802
Raskin, C., Scannapieco, E., Fryer, C., Rockefeller, G., & Timmes, F. X. 2012, ApJ, 746, 62
Robson, T., Cornish, N. J., & Liu, C. 2019, CQGra, 36, 105011
Roy, N., Tiwari, V., Bobrick, A., et al. 2022, arXiv:2204.09683
Rueda, J., Ruffini, R., Wang, Y., et al. 2019, JCAP, 2019, 044
Ruiter, A. J., Ferrario, L., Belczynski, K., et al. 2019, MNRAS, 484, 698
Sana, H., de Mink, S. E., de Koter, A., et al. 2012, Science, 337, 444
Sato, Y., Nakasato, N., Tanikawa, A., et al. 2015, ApJ, 807, 105
Sato, Y., Nakasato, N., Tanikawa, A., et al. 2016, ApJ, 821, 67
Schwab, J. 2021, ApJ, 906, 53
Schwab, J. 2021, ApJ, 906, 53
Seitenzahl, I. R., Herzog, M., Ruiter, A. J., et al. 2015, PhRvD, 92, 124013
Shen, K. J. 2015, ApJL, 805, L6
Strumia, A., & Vissani, F. 2003, PhLB, 564, 42
Toonen, S., Nelemans, G., & Portegies Zwart, S. 2012, A&A, 546, A70
Vitagliano, E., Tamborra, I., & Raffelt, G. 2020, RvMP, 92, 045006
Wagg, T., Breivik, K., & de Mink, S. E. 2021, arXiv:2111.08717
Wolfenstein, L. 1978, PhRvD, 17, 2369
Wright, W. P., Kneller, J. P., Ohlmann, S. T., et al. 2017, PhRvD, 95, 043006
Wu, C., Xiong, H., & Wang, X. 2022, MNRAS, 512, 2972
Xiao, D., Mészáros, P., Murase, K., & Dai, Z.-G. 2016, ApJ, 832, 20
Yu, S., & Jeffery, C. S. 2010, A&A, 521, A85
Yungelson, L. R., & Kuranov, A. G. 2016, MNRAS, 464, 1607
Zou, Z.-C., Zhou, X.-L., & Huang, Y.-F. 2020, RAA, 20, 137
Zyla, P., Barnett, R. M., Beringer, J., et al. 2020, PTEP, 2020, 083C01